Separation and Purification Technology 405 (2026) 138925

Contents lists available at ScienceDirect

Separation and Purification Technology

journal homepage: www.elsevier.com/locate/seppur

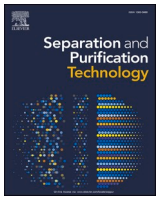

An interface-coated electrostatic precipitator for particulate matter removal across particle sizes and compositions: Principles, design, and experimental evaluation

Xihui Liu [b], Wuwei Zou [b], Guoqing Cao [c], Zhaowei Xu [c], Jinhan Mo [a,b,d,e,*]

[a] Key Laboratory of Coastal Urban Resilient Infrastructures (Ministry of Education), College of Civil and Transportation Engineering, Shenzhen University, Shenzhen 518060, China
[b] Beijing Key Laboratory of Indoor Air Quality Evaluation and Control, Department of Building Science, Tsinghua University, Beijing 100084, China
[c] Institute of Building Environment and Energy, China Academy of Building Research, Beijing 100013, China
[d] State Key Laboratory of Subtropical Building and Urban Science, Shenzhen University, Shenzhen 518060, China
[e] Key Laboratory of Coastal Urban Soil-Water Environmental Evolution, Ministry of Ecology and Environment (under construction), Shenzhen University, Shenzhen 518060, China

ARTICLE INFO

Keywords:
Electrostatic precipitation
Dielectric-coated electrode
Breakdown voltage
Particle dielectric property
Broad-spectrum removal

ABSTRACT

Electrostatic precipitators (ESPs) are widely recognized as cost-effective air purification technologies. However, achieving high and broad-spectrum removal efficiency across diverse particle sizes and compositions remains a persistent challenge. In this study, an electrostatic precipitator featuring dielectric-coated collecting electrodes was developed, and its removal performance for particulate matter (PM) with varying sizes and compositions was systematically evaluated. Experimental results demonstrated that the polyethylene terephthalate (PET) coating increased the breakdown voltage by up to 1.8 times, thereby enabling higher operating safety and enhanced removal efficiency. A theoretical framework was established to quantify the distinct contributions of geometric and electrohydrodynamic effects to efficiency enhancement, utilizing the dimensionless effective area (A^*) and migration velocity (u^*). Broad-spectrum performance was validated using five representative particle types (NaCl, Fe, Fe_2O_3, DEHS, and indoor ambient particles), achieving a removal efficiency of up to 99.9% at a collecting voltage of 1 kV. Long-term tests with DEHS particles further demonstrated stable operation and complete recovery of efficiency after washing. This study provides a viable solution and a systematic framework for the safe, economical, high-performance, and broad-spectrum removal of airborne particulate matter, offering strong potential for practical indoor air purification applications.

1. Introduction

Airborne particulate matter (PM) poses a serious threat to human health worldwide, and the situation remains increasingly concerning [1]. Exposure to PM, especially fine particles with larger surface area and high penetrability, is strongly associated with respiratory and cardiovascular diseases, cognitive impairment, and increased premature mortality, even at low concentrations [2–5]. Despite worldwide attention and substantial mitigation efforts, the health burden of PM continues to rise annually [6]. The prolonged indoor occupancy of the population (nearly 90% of their time spent indoors) highlights the need for efficient indoor PM removal strategies in building ventilation systems [7,8].

Among available PM control technologies, the cost-effective electrostatic precipitator (ESP) method stands out for its low pressure drop, high airflow capacity, and reusability. Generally, it falls short of high-efficiency particulate air (HEPA) filters in achieving ultra-high removal efficiency [9–11]. The development of highly efficient and broadly effective ESP remains a primary pursuit in numerous studies. The determinants of efficiency can be categorized into two primary dimensions: design and operational parameters, and the physicochemical properties of PM.

Several studies have explored altering the structure of the collection electrodes. Zhu et al. [12,13] developed a corrugated plate electrostatic

* Corresponding author at: Key Laboratory of Coastal Urban Resilient Infrastructures (Ministry of Education), College of Civil and Transportation Engineering, Shenzhen University, Shenzhen 518060, China.
E-mail address: mojinhan@szu.edu.cn (J. Mo).

https://doi.org/10.1016/j.seppur.2026.138925
Received 23 April 2026; Received in revised form 4 June 2026; Accepted 12 June 2026
Available online 13 June 2026

precipitator (CP ESP), which exhibited enhanced electrostatic field characteristics compared to a parallel plate ESP. In addition to the corrugated electrode structure, other structural designs aimed at enhancing airflow field disturbance include square-wave electrodes [14], perforated electrodes [15], and the incorporation of baffles [16]. However, these structural modifications increase geometric complexity and may generate strong localized vortices, leading to secondary particle resuspension. Optimizing particle migration primarily relies on strengthening the electric field by increasing the voltage or reducing the electrode spacing [17,18]. However, these approaches are often constrained by safety considerations related to electric sparks [19–21]. To overcome the breakdown limitation of conventional ESPs under high electric fields, Mo et al. [21,22] introduced unilateral dielectric-coated electrodes to increase the breakdown threshold while maintaining high particle collection efficiency. However, several key issues remain unresolved. A systematic theoretical framework for interpreting coating-induced enhancement mechanisms and guiding coated-ESP optimization has not yet been established. In addition, systematic evaluation of coating performance under different electrode spacings, discharge conditions, and particle properties remains limited, requiring further validation of its general applicability.

Regarding particle-side characteristics, particle size is the most critical determinant of ESP performance, with collection efficiency typically reaching a minimum in the 0.1–0.5 μm range, while some studies have also reported a minimum around 0.01 μm [17,23]. Owing to the higher capture efficiency for coarse particles, various coagulation-based strategies, including thermophoretic [24], chemical [25], acoustic [26], and turbulent [27] methods, have been proposed to promote particle growth and enhance collection. However, these approaches often increase system complexity and hinder practical implementation. In addition, the electrical conductivity and phase state of particulate matter can also significantly influence collection efficiency. There have been studies investigating ESP performance for kitchen oil fumes (liquid particles) [28,29], bacteria and viruses [30–33], combustion-generated dust from different types of biomass (e.g., spruce, beech, straw, and sunflower) [34], and welding fumes [35]. However, existing studies are scattered across different experimental setups and operating conditions, resulting in limited comparability, with many investigations relying solely on numerical simulations, highlighting the need for systematic experimental investigations under unified operating conditions.

To address these challenges, this study develops an interface-coated electrostatic precipitator to achieve high-performance and broad-spectrum particulate matter removal. A theoretical framework is established to quantitatively analyze the roles of the dimensionless effective area (A^*) and the electrohydrodynamic parameter (u^*) in efficiency enhancement. PET-coated collecting electrodes with variable electrode spacing are fabricated to increase the breakdown voltage and expand the operational electric field range. The removal performance is systematically evaluated across particle sizes and compositions using representative aerosols, including sodium chloride (NaCl), iron (Fe), iron oxide (Fe_2O_3), di-ethylhexyl sebacate (DEHS), and indoor ambient particles. A removal efficiency of up to 99.9% was achieved at a collecting voltage of 1 kV for all particle sources. This work aims to provide a comprehensive understanding of particle–device interactions and a systematic framework for the design and performance evaluation of high-efficiency ESP systems with broad-spectrum effectiveness.

2. Methods

2.1. Theoretical analysis

A typical electrostatic particle capture process involves two steps: particle charging and electrode collecting within the electric field. In terms of particle capture performance under a given airflow, the efficiency is determined by two major categories: the intrinsic properties of the particulate matter and the device parameters, including geometrical dimensions and electrical inputs, as illustrated in Fig. 1. The factors influencing the efficiency and the strategies for its improvement are presented below.

In the charging process, mechanisms include field charging through ion bombardment and diffusion charging through ion diffusion [9]. Various models have been proposed to describe this process [36], which can generally be classified into two categories: models predicting a saturated charge, such as the well-known White model, and models describing particle charge as a time-dependent function obtained by summing the contributions of field charging and diffusion charging. Among these models, the Cochet model modifies the electric field distribution on particle surfaces, improving the prediction accuracy for submicron particles. The Cochet equation is employed here to approximate the combined effects of diffusion charging and field charging and is empirically expressed by **Eq.(1)** [37]. Notably, the differences in charging performance among various particles are expected to be attributed to their diameters and dielectric constants.

$$q = \pi\varepsilon_0 E_c d_p^2 \left[\frac{\varepsilon_p - 1}{\varepsilon_p + 2} \frac{2}{1 + \frac{2\lambda}{d_p}} + \left(1 + \frac{2\lambda}{d_p}\right) \right] \tag{1}$$

where, q is the particle charge (C); ε_0 is the vacuum permittivity (8.85×10^{-12} F/m); E_c is the electric field strength during the charging process (V/m); d_p is the particle diameter (m); ε_p is the relative dielectric constant of the particle; λ is the mean free path of gas molecules (m).

After charging, particles migrate in the electric field between the electrodes and are ultimately collected. The migration velocity u_e is the key parameter determining the efficiency. According to the classical Stokes' drag law, the migration velocity of particles emerging from a balance of drag force and electric force is as follows:

$$u_e = \frac{qE}{3\pi\mu d_p} \tag{2}$$

where, μ is the coefficient of dynamic viscosity (Pa·s), E is the intensity of the collecting electric field (V/m).

According to Eq.(2), when considering the influence of particle properties on the migration velocity, the charge-to-diameter ratio q/d_p can be regarded as an intrinsic parameter. However, the Stokes' drag law significantly overestimates the fluid resistance for sub-micron particles; thus, the Cunningham slip correction factor (C_c) must be introduced to accurately calculate the resistance for fine particles. According to the Cunningham-corrected Stokes' Law, the migration velocity can be rewritten as follows:

$$u_e = \frac{qC_c}{d_p} \frac{E}{3\pi\mu} \tag{3}$$

$$C_c = 1 + \frac{2\lambda}{d_p}\left[A + B\cdot\exp\left(-C\frac{d_p}{2\lambda}\right)\right] \tag{4}$$

where, C_c is the Cunningham correction coefficient, the constants are: $A = 1.246$, $B = 0.42$, $C = 0.87$ [38,39].

At a given collecting electric field, u_e is determined by $C_c \cdot q/d_p$. Consequently, a C_c modified charge-to-diameter ratio is proposed as a refined metric that integrates the coupled effects of particle charging behavior and particle dynamics for submicron particles, as defined below:

$$C_c \text{ modified charge-to-diameter ratio} = \frac{qC_c}{d_p} \tag{5}$$

For efficiency improvement, a dimensionless efficiency model was developed based on the classical Deutsch framework as an engineering approximation to decouple geometric and electrohydrodynamic effects for design interpretation. The assumptions are: (1) particle

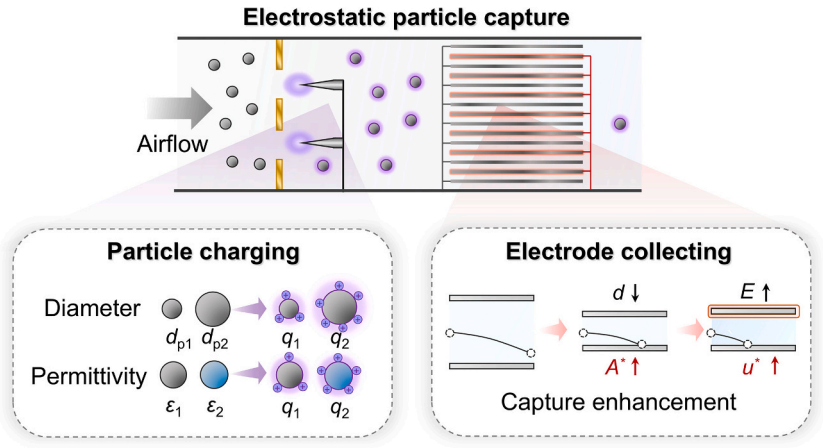

Fig. 1. Illustration of the charging and collecting processes in electrostatic particle capture, the factors influencing efficiency, and strategies for performance improvement.

concentration varies only in the streamwise direction, and the cross-sectional average concentration is used as the effective local concentration, i.e.,$C = \overline{C}(x)$; the boundary layer near the collecting plate is neglected; (2) the migration velocity of particles toward the collecting plate is assumed to be constant, and gravitational effects are ignored; (3) collection is assumed to be complete upon particle deposition on the plate, with re-entrainment neglected. The dimensionless efficiency is expressed as follows:

$$\eta = 1 - \exp\left(-\frac{u_e L}{u_\infty H}\right) = 1 - \exp(-u^* \cdot A^*) \tag{6}$$

$$A^* = \frac{A_c}{A_f} \tag{7}$$

$$u^* = \frac{u_e}{u_\infty} \tag{8}$$

where, A_c is the area of the collecting electrode (m^2); A_f is the cross-sectional area of the flow channel between collecting electrodes (m^2); A^* is the dimensionless effective area, the ratio of the collecting area to the flow channel area, dimensionless; u_∞ is the mainstream velocity (m/s); u^* is the dimensionless effective migration velocity, the ratio of the migration velocity to the mainstream velocity, dimensionless.

According to this dimensionless efficiency model, the performance enhancement of the ESP can be attributed to increasing the dimensionless effective area A^* (representing geometrical enhancement) and increasing the dimensionless effective migration velocity u^* (representing electrohydrodynamic enhancement). Practically, these can be achieved by reducing the electrode spacing and increasing the electrode electric field strength.

Here, an evaluation method is further developed to quantitatively distinguish the contributions of A^* and u^* between two operating conditions. The performance difference can be decomposed through logarithmic analysis of the governing parameter $A^* \cdot u^*$. By taking the natural logarithm of the ratio of this parameter before and after enhancement, Eq.(9) is obtained with the assumption of identical mainstream conditions. After a mathematical transformation, as shown in Eq.(10), the relative contributions of geometrical enhancement A^* and electrohydrodynamic enhancement u^* can be quantified as expressed in Eq. (11).

$$\ln\frac{A_2^* \cdot u_2^*}{A_1^* \cdot u_1^*} = \ln\frac{A_2^*}{A_1^*} + \ln\frac{u_2^*}{u_1^*} \tag{9}$$

$$\frac{\ln\frac{A_2^*}{A_1^*}}{\ln\frac{A_2^* \cdot u_2^*}{A_1^* \cdot u_1^*}} + \frac{\ln\frac{u_2^*}{u_1^*}}{\ln\frac{A_2^* \cdot u_2^*}{A_1^* \cdot u_1^*}} = 1 \tag{10}$$

$$\Delta\eta = \Delta\eta_{A^*} + \Delta\eta_{u^*} = \Delta\eta\frac{\ln\frac{A_2^*}{A_1^*}}{\ln\frac{A_2^* \cdot u_2^*}{A_1^* \cdot u_1^*}} + \Delta\eta\frac{\ln\frac{u_2^*}{u_1^*}}{\ln\frac{A_2^* \cdot u_2^*}{A_1^* \cdot u_1^*}} \tag{11}$$

where, $\Delta\eta$ represents the increase in efficiency, which can be decomposed into two terms on the right side of the equation: the first term corresponds to the improvement associated with A^*, and the second term corresponds to that associated with u^*. Therefore, the enhancement in particle capture performance due to geometrical and electrohydrodynamic effects can be evaluated separately.

2.2. PET-coated collecting electrode unit fabrication

Commercially available stainless-steel plates (200 μm thick) were sectioned into collecting electrodes with dimensions of 7 cm × 6 cm. A 70 μm thick PET film was coated onto a galvanized iron electrode via a roll-to-roll thermal pressing process to fully encapsulate the original electrode. This dielectric coating on the electrode provides a modified surface and reduces electron emission, thereby increasing the breakdown voltage. The detailed procedure was consistent with that reported in our previous study [22].

Bare and coated electrodes were alternately assembled using a magnetic assembly method to construct the collecting electrode unit, serving as the ground and high-voltage electrodes, respectively. The electrode spacing was varied to 1, 2, 3, 4, and 5 mm.

2.3. Experimental setup and testing procedures

A lab-scale air duct setup (cross-section 8 × 8 cm) was constructed for performance testing (Fig. 1). Two high-voltage power supplies (P30, Boer Co., Ltd., Suqian, China) with direct current output were employed to independently power the sequential pin-to-plate charging unit and the collecting electrode unit. Particle number concentrations for sizes 0.3–10 μm and below 0.3 μm were measured using a particle counter (Aerotrak 9306, TSI Inc., Shoreview, USA) and a scanning mobility particle sizer (NanoScan SMPS 3910, TSI Inc., Shoreview, USA), respectively. Details are stated in Supplementary Methods S1.

To evaluate the broad-spectrum effectiveness of the ESP, five representative particle sources with diverse physicochemical properties were selected and tested: NaCl, Fe, Fe_2O_3, DEHS, and indoor ambient particles. All single-component aerosols were generated using a

nebulizer (MRE 6Jet, BGI Inc., USA). NaCl, Fe, and Fe_2O_3 were dispersed in deionized water, while DEHS was dispersed in ethanol. The validity of this approach was experimentally verified: particle concentrations generated from pure ethanol were negligible, whereas a significant increase in particle number concentration was observed after adding DEHS, confirming that the measured aerosols originated primarily from DEHS rather than the solvent. Detailed validation results are provided in Supplementary Fig. S1.

2.4. Characterization

After particle deposition for 2.5 h in the ESP system, the collecting electrode plate was sectioned and sampled, and the morphology of the deposited particulate matter was examined using a field-emission scanning electron microscope (FE-SEM, Merlin VP Compact, Carl Zeiss AG).

3. Results and discussion

3.1. ESP performance leverage effect

Applying a dielectric coating to the collecting plate is expected to increase the breakdown voltage. Using a roll-to-roll thermal pressing method, PET-coated collecting electrodes were successfully prepared, and the cross-sectional SEM image is shown in Supplementary Fig. S2, revealing a clear hierarchical structure and strong adhesion. The coating film was several millimeters larger than the edge of the collecting plate to thoroughly envelop the plate and reliably increase the breakdown voltage.

The breakdown voltage as a function of electrode spacing, with and without the coating, is shown in Fig. 2(a). Notably, all breakdown voltages with the PET coating were consistently higher than those of the bare electrodes. At an electrode spacing of 1 mm, the breakdown voltage increased from 2.2 to 3.5 kV after coating. As the electrode spacing was increased to 5 mm, the breakdown voltage reached 5.5 kV for bare electrodes and could be elevated to 10.3 kV with the coating. On average, coating the electrode increased the breakdown voltage by 1.8 times that of the bare electrode. This leverage in breakdown voltage yields the benefit of electrical safety and increases the upper limit of the applied voltage.

Fig. 2(b) illustrates the removal efficiency of 0.3–0.5 μm particles under varying collecting voltages and electrode spacings, with the charging voltage fixed at 7 kV, revealing the effects of reduced electrode spacing and increased collecting voltage. At a collecting voltage of 1 kV, the efficiency increased significantly from 46.9% to 93.6% as the electrode spacing reduced from 5 to 1 mm. Furthermore, when the collecting voltage was raised from 0.5 to 3 kV at an electrode spacing of 2 mm, the efficiency improved from 44.0% to 95.8%.

The improvement in particle removal performance can be quantitatively attributed to two factors: geometrical and electrohydrodynamic effects, represented by A^* and u^*, respectively. These two parameters were analyzed to quantify their respective contributions to performance enhancement through both experimental data and theoretical calculations, as shown in Fig. 2(c). The theoretical results were obtained by Eq. (11). To quantitatively evaluate the accuracy of the decoupled efficiency increment between experimental and theoretical results, statistical goodness-of-fit indicators, including mean absolute error (MAE), root-mean-square error (RMSE), and coefficient of determination (R^2), were introduced. The calculated values of MAE, RMSE, and R^2 are 0.030, 0.031, and 0.859, respectively, indicating reasonably good agreement. A detailed comparison between experimental and theoretical decoupled efficiency increments is further provided in Supplementary Fig. S3. In the performance comparison between 5 mm and 1 mm electrode spacing at 1 kV collecting voltage, the increase in efficiency from 46.9% to 93.6% could be attributed to A^* and u^*, whose contributions were 26.8% and 29.9% experimentally, and 23.4% and 23.4% theoretically.

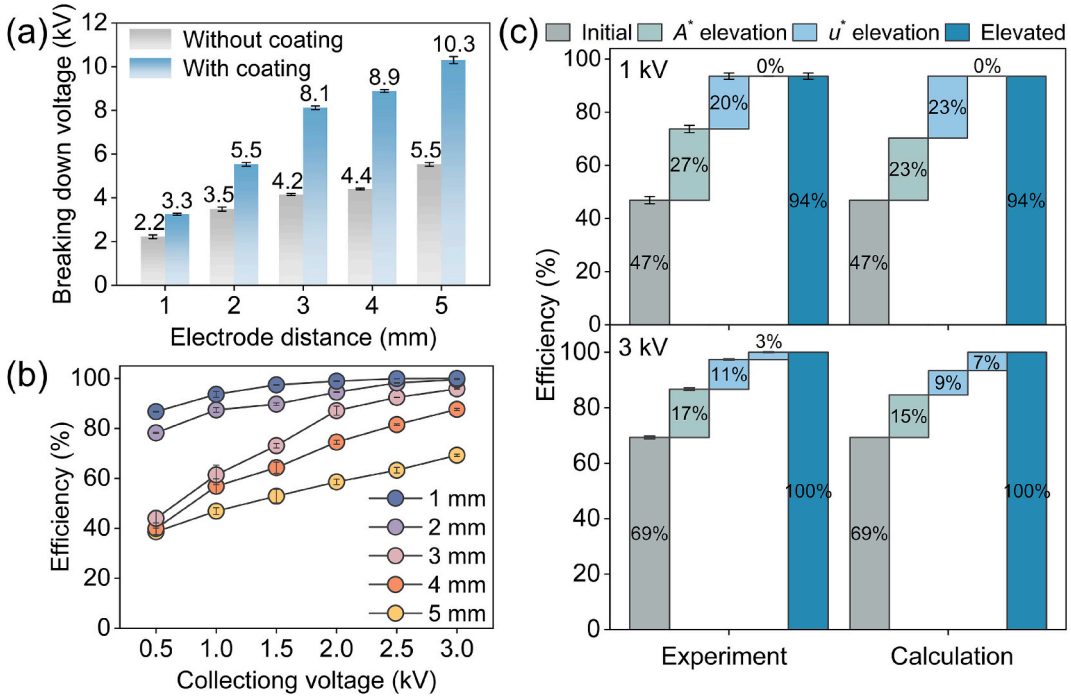

Fig. 2. (a) Breakdown voltage versus electrode spacing. The environmental conditions were 22 °C and 12% relative humidity. The error bars represent the standard deviation of three measurements. (b) Collecting efficiencies for 0.3–0.5 μm particles under a 7 kV charging voltage and a 1 m/s face velocity. All error bars of efficiencies represent the standard deviation of five continuous measurements. (c) The contributions of A^* and u^* to the efficiency enhancement. The u^* increment is partitioned by the breakdown voltage of the bare collecting electrode: the first and second columns represent the increase before and after the breakdown voltage enhancement due to the coated collecting electrodes, respectively. The conditions were a 7 kV charging voltage and collecting voltages of 1 kV and 3 kV, with electrode spacing ranging from 5 mm to 1 mm.

The results of theoretical calculations and experiments showed good agreement. With the collecting voltage held constant and the electrode spacing reduced, the geometrical effect A^* and electrohydrodynamic effect u^* contribute equally to the efficiency increase in theory. Furthermore, at higher collecting voltages, particularly as the voltage approaches the breakdown threshold of the collecting electrode, the electrode coating can facilitate a larger increase in u^* compared with the bare electrode. Specifically, under initial conditions of a 3 kV collecting voltage and a 5 mm electrode spacing, the maximum contribution of u^* to the efficiency was 8.7%. With the coating applied to the collecting electrode, u^* could theoretically contribute an additional efficiency increment of 6.6%. The coating on the collecting electrode enhances the attainable maximum efficiency.

As we have proposed, the particle capture efficiency of the ESP can be enhanced by increasing two dimensionless parameters: the geometrical parameter A^* and the electrohydrodynamic parameter u^*. However, in practical applications, increases in both parameters are inherently constrained by the trade-off effect, as shown in Fig. 3(a). As the parameter u^* increases, the electric field progressively approaches the breakdown limit, leading to electrical sparks and posing significant operational safety concerns. This upper limit can be substantially extended through electrode coating, unlocking a great potential of u^*. To enhance the geometrical parameter A^*, air resistance increases due to narrower flow channels and electrode cross-section blockage, resulting in a trade-off.

Higher A^* leads to improved removal efficiency at the cost of increased pressure drop, accompanied by an additional energy penalty. To evaluate the trade-off between efficiency and pressure drop, the pressure drop of the collecting electrode unit was first experimentally characterized under various face velocities and electrode spacings, as presented in Fig. 3(b). Specifically, the pressure drop across the 3 mm electrode-spacing collecting unit ranged from 3.0 to 17.5 Pa, with face velocity adjusted from 0.5 to 3 m/s. As the electrode spacing decreases, the pressure drop showed a nonlinear increase; for example, at 2 m/s, altering the electrode spacing from 3 mm to 5 mm and 1 mm led to pressure drops of 9.0 and 18.6 Pa, respectively, indicating that spacing reduction at smaller electrode spacing induces disproportionately higher air resistance increases. Therefore, striking a balance between air resistance and particle removal performance is essential.

To quantitatively characterize the optimal balance between air resistance and particle removal performance, we proposed normalized parameters to compare the costs and rewards, as illustrated in Fig. 3(c). The normalized efficiency (η/η_0) and air resistance (P/P_0) were defined to evaluate the efficiency reward and the pressure drop cost associated with reducing electrode spacing, where the reference point (η_0, P_0) corresponds to a 7 kV charging voltage, 1 m/s face velocity, and 5 mm electrode spacing. Generally, the normalized efficiency-resistance curve exhibited a rapid initial increase followed by a gradual rise toward an upper limit. As a representative case, narrowing the electrode spacing to 2 mm results in a normalized efficiency (η/η_0) of 1.86 with P/P_0 of 1.75, while further reducing it to 1 mm yields a η/η_0 of 1.99 with P/P_0 of 3.12, indicating a marginal efficiency reward accompanied by a substantial increase in air resistance. In addition, the upper limit of η/η_0 decreased as the collecting voltage and particle diameter increased. The highest η/η_0 of 1.99 was achieved at a collecting voltage of 1 kV for 0.3–0.5 μm particles, while a lower value of 1.56 was observed for 0.5–1 μm particles, and a value of 1.68 was obtained at a collecting voltage of 2 kV. Based on the above analysis, a 2 mm electrode spacing is recommended to strike a balance between particle removal efficiency and air resistance if energy costs are taken into consideration.

In addition, an energy-efficiency analysis was performed. We compared the proposed ESP with existing air purification technologies, including HEPA filters and conventional ESP systems, in terms of total power consumption (P), clean air delivery rate ($CADR$), and energy consumption per unit clean air delivery rate (E_{CADR}). Detailed data are provided in the Supplementary Methods S2. Benefiting from the low pressure drop and high particle removal efficiency, the proposed system exhibits the lowest E_{CADR} of 37.34 J/m^3, highlighting its superior energy-performance trade-off and practical applicability for real-world air purification.

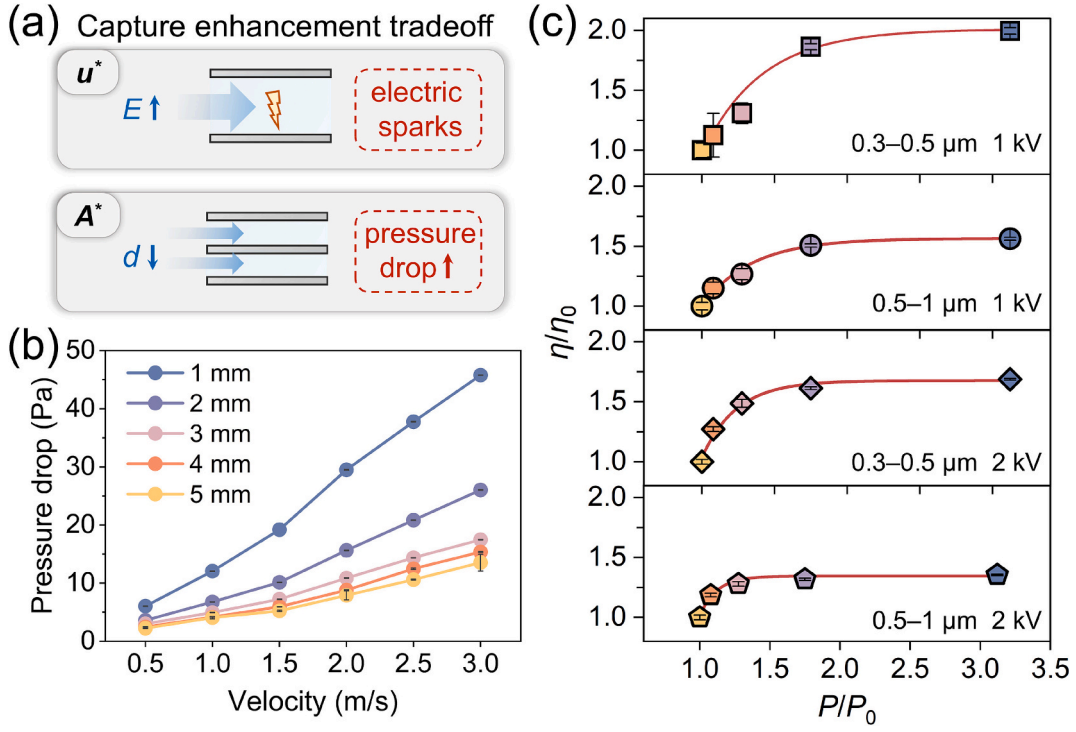

Fig. 3. (a) The trade-off effect of particle capture efficiency enhancement by A^* and u^*. (b) The pressure drop of the collecting electrode unit under various face velocities and electrode spacings. (c) The normalized efficiency η/η_0 and normalized resistance P/P_0 of the collecting electrode unit. The reference point (η_0, P_0) corresponds to a 7 kV charging voltage, 1 m/s face velocity, and 5 mm electrode spacing. Data point colors correspond to those in (b).

3.2. Removal performance of different particle sizes

In addition to the geometric and electrical properties of the ESP, particle capture efficiency is significantly influenced by intrinsic particle characteristics, particularly particle diameter. Particle diameter primarily affects efficiency by influencing particle charge and its motion within the airflow and electric field. These two aspects are analyzed in Fig. 4(a). According to Eq. (1), the charge acquired by particles with diameters ranging from 0.01 to 10 μm is calculated theoretically, showing a non-linear increase as particle size transitions from the submicron to the micron scale. This phenomenon is primarily attributed to the shift from diffusion charging to field charging, which scales with the square of the particle diameter. This substantial charge accumulation essentially dictates the superior collection efficiency of ESP for larger particles. As analyzed in Section 2.1, two additional parameters can be used to characterize the effect of particle diameter on efficiency. Considering the dynamics of particle motion, the charge-to-diameter ratio q/d_p exhibits a subtle localized enhancement near 10 nm. However, this remains insufficient to accurately characterize sub-micron particle efficiency. In contrast, the proposed modified charge-to-diameter ratio $C_c \cdot q/d_p$ exhibits a distinct U-shaped trend, with a global minimum at approximately 0.2 μm. This aligns closely with the widely reported efficiency valley for 0.1–5 μm particles [10,23]. Thus, the proposed $C_c \cdot q/d_p$ parameter provides a robust characterization of size-dependent particle removal performance.

Fig. 4(b) illustrates the ESP removal efficiency as a function of particle diameter and collecting voltage. High efficiencies were observed for both ultrafine (<0.3 μm) and large (>3 μm) particles, while a pronounced minimum occurred within the 0.3–0.5 μm interval. Specifically, at a collecting voltage of 0.1 kV, the efficiency for 0.3–0.5 μm particles was 54.2%, while remaining 94.1% for particles larger than 5 μm. This size-dependent efficiency distribution is consistent with the trend characterized by $C_c \cdot q/d_p$. The removal performance exhibited a positive correlation with the collecting voltage. Notably, at a collecting voltage of 0.5 kV, high removal efficiencies were consistently maintained across the entire particle size range, with a minimum value of 97.1%, demonstrating highly effective particle capture.

3.3. Removal performance of different particle compositions

Five representative particle types, including NaCl, Fe, Fe_2O_3, DEHS, and indoor ambient particles, was employed to evaluate the broad-spectrum collection performance of the ESP. These sources were chosen to represent the complex physicochemical characteristics found in real-world particulate matter. NaCl was employed as a standard test aerosol commonly used in laboratory studies of particulate matter removal [40,41]. Fe and Fe_2O_3 represented typical metallic and metal oxide constituents in underground environments, such as subway systems, where iron-containing particles primarily originate from rail-wheel wear [42–44]. DEHS, a single-component, non-volatile liquid, can be readily atomized into stable aerosols and exhibits aerodynamic behavior similar to cooking oil droplets [45,46]. It was selected to represent liquid oil aerosols associated with cooking emissions and other organic compound sources. Indoor ambient particles were directly sampled from our laboratory without artificial generation, representing a realistic mixed composition.

As shown in Fig. 5(a), SEM images of solid-phase particles deposited on the ESP collecting electrode reveal distinct morphological features for particles from different sources. NaCl particles exhibit cubic crystal structures with smooth surfaces and sharp edges. Fe particles present irregular, aggregated morphologies with rough surfaces, mainly resulting from mechanical fragmentation and strong inter-particle adhesion driven by high surface energy [47–49]. Iron oxide particles are predominantly spherical. Indoor ambient particles exhibit highly heterogeneous, irregular structures, reflecting their complex composition.

The variations in removal performance across the different particle types are illustrated in Fig. 5(b). While indoor ambient particles showed variable results, the remaining four particle sources exhibited a virtually identical ranking in collection efficiency across most tested conditions and particle diameter ranges, in descending order of Fe, Fe_2O_3, NaCl, and DEHS. For instance, at 7 kV charging voltage and 0.2 kV collecting voltage, the 0.3–0.5 μm removal efficiencies for Fe, Fe_2O_3, NaCl, and DEHS were 88.9%, 87.6%, 83.0%, and 75.5%, respectively, while that of indoor ambient particles was 91.7%. The Fe, Fe_2O_3, NaCl, DEHS, and indoor ambient particles exhibit distinct dielectric properties, with relative dielectric constants of ∞ (conductor), 14.2, 5.9, 2.5, and 2–10, respectively [50–53]. For particles with the same diameter but different compositions, their kinetic behavior is consistent; the primary distinction lies in their charge quantity, which is fundamentally determined by the dielectric constant. According to Eq.(1), the charges of the single-component particles were calculated and are presented in Fig. 5(c). The particle charge exhibits a strong dependence on both particle diameter and composition. The influence of dielectric constant on particle charging, particularly for ultrafine particles, is negligible, whereas

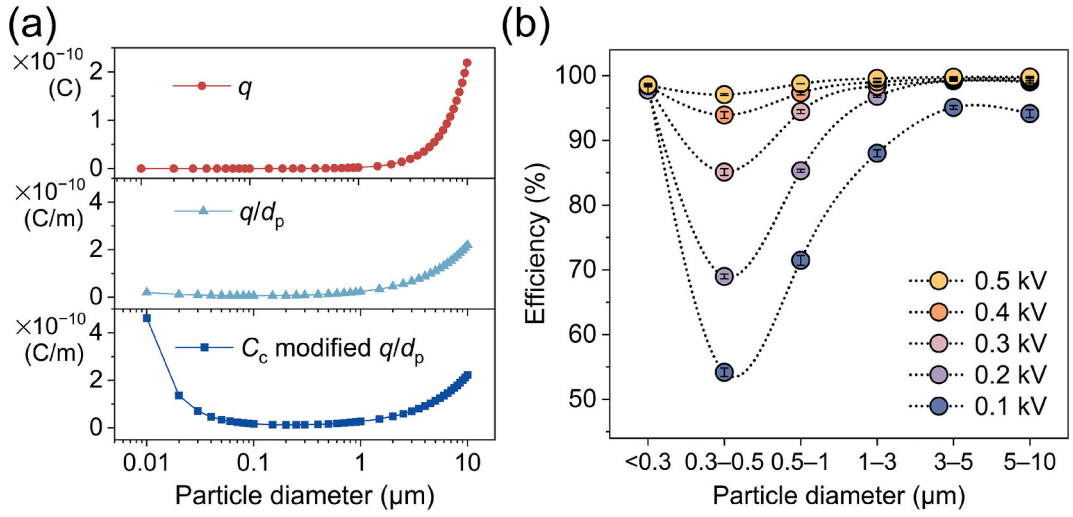

Fig. 4. (a) Particle charge (C), charge-to-diameter ratio (C/m), and modified charge-to-diameter ratio (C/m) as functions of particle diameter. The conditions are a 7 kV charging voltage and a relative dielectric constant of 5.9 (NaCl particles). (b) Particle removal efficiency versus particle diameter and collection voltage at a 7 kV charging voltage, 1 m/s face velocity, and 1 mm electrode spacing.

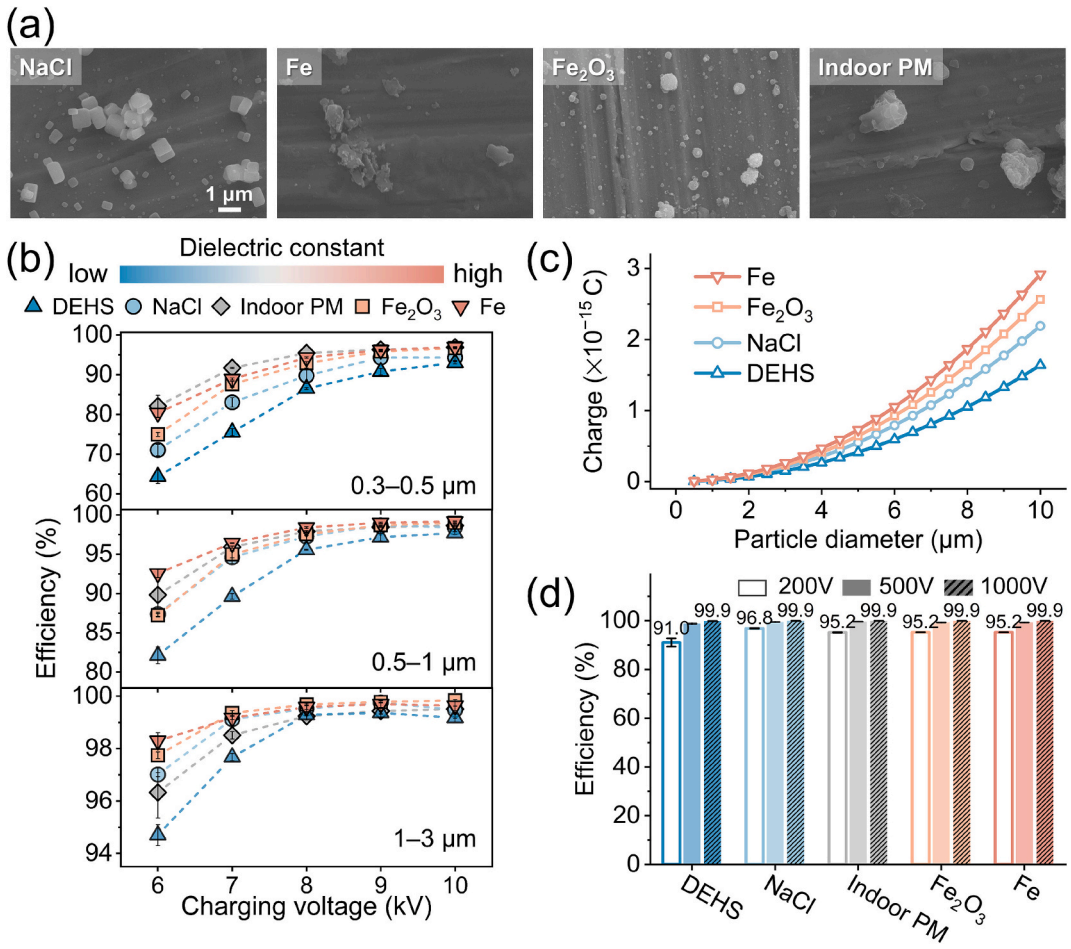

Fig. 5. (a)SEM images of solid-phase particles deposited on the ESP collecting electrode (from left to right: NaCl, Fe, Fe_2O_3, and indoor ambient particles). (b) Particle removal efficiency for five particle sources (NaCl, Fe, Fe_2O_3, DEHS, and indoor ambient particles) at a 0.2 kV collecting voltage, 1 m/s face velocity, and 1 mm electrode spacing. (c) Particle charge of four single-component particle sources (NaCl, Fe, Fe_2O_3, and DEHS) at a 7 kV charging voltage. (d) Particle removal efficiency of 0.3–0.5 μm versus collecting voltage at a 10 kV charging voltage, 1 m/s face velocity, and 1 mm electrode spacing.

its effect becomes more pronounced for larger particles. Notably, at any given diameter, the charge values follow a descending order of Fe, Fe_2O_3, NaCl, and DEHS, which closely aligns with their respective dielectric constants and removal performance. Regarding indoor ambient particles, the variations in the efficiency ranking across different diameter intervals are likely attributable to their heterogeneous composition. The detailed particle size distribution within a specific interval also influences the corresponding removal efficiency.

The 0.3–0.5 μm particle removal performance under a charging voltage of 10 kV was subsequently evaluated across a range of collecting voltages, with results detailed in Fig. 5(d). A positive correlation between collecting voltage and removal efficiency was observed across all particle sources, and the differences among sources diminished as the voltage increased. At a collecting voltage of 1 kV, an exceptionally high removal efficiency of 99.9% was consistently achieved for all particle sources, including heterogeneous indoor ambient particles and single-component particles. This uniform high-performance capability underscores the robustness of the ESP in effectively treating a wide range of particulate matter.

3.4. Long-term performance

The long-term performance and post-washing reusability of an ESP are critical for real-world applications. Ozone generation was monitored at both the upstream and downstream of the ESP unit, as shown in Supplementary Fig. S4. At a charging voltage of 7 kV, ozone generation remained low, with an outlet concentration of 15.8 ppb, indicating stable operation of the four-pin corona discharge array. When the voltage increased, a pronounced rise in ozone production was observed, reaching 45.7 ppb at 10 kV. The average background ozone level was 14.5 ppb. For reference, the WHO 8-h mean air quality guideline for ozone is 100 $\mu g/m^3$ (approximately 47 ppb) [54]. Relative to this threshold, only the operating conditions at 9 and 10 kV resulted in exceedance at the ESP outlet, where ozone concentrations reached 49.4 and 60.2 ppb. A continuous two-week experiment was conducted with a charging voltage of 7 kV, which was intentionally kept relatively low to mitigate ozone generation. Considering the unique properties of oil particles, liquid and viscous, DEHS was selected as the long-term particle source. The results are presented in Fig. 6. The typical daily PM source concentration is shown in Supplementary Fig. S5, with concentrations of 1.6×10^5 #/L for 0.3–0.5 μm, 1.1×10^5 #/L for 0.5–1 μm, and 5.6×10^4 #/L for 1–3 μm particles. The environmental parameters, including temperature and relative humidity during the long-term test, are summarized in Supplementary Table S4.

In general, the long-term performance deterioration of ESP stems from several fundamental mechanisms. The accumulation of a dust cake on the collection plates inevitably triggers back corona discharge within the layer [55]. Furthermore, aerodynamic shearing aggravates the re-entrainment and resuspension of already captured particles [56]. On the discharge side, particulate fouling leads to the passivation and blunting of emission electrode tips, which subsequently reduces the overall corona discharge stability during extended operational periods

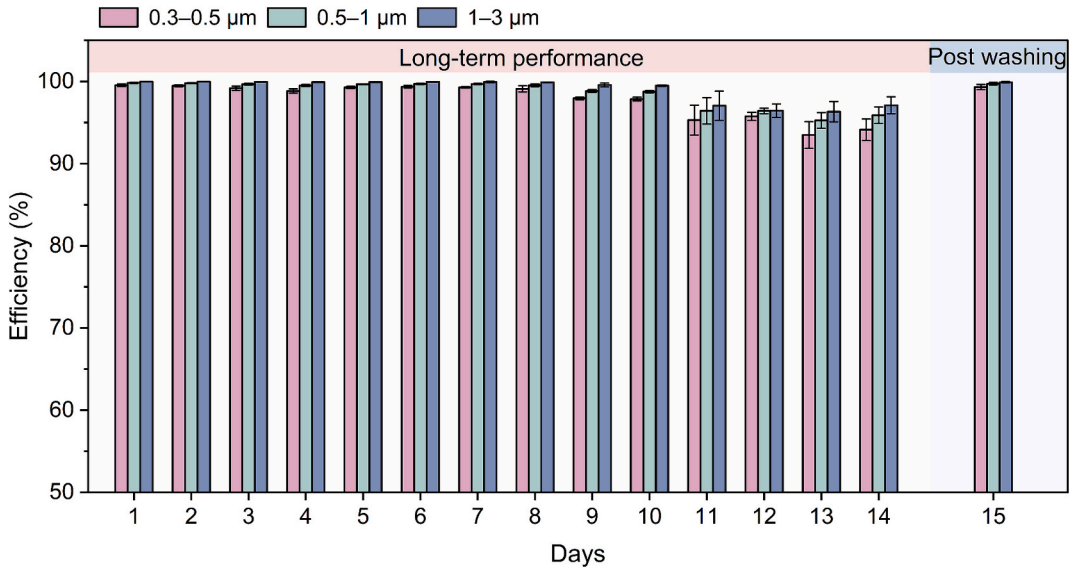

Fig. 6. Long-term ESP performance for DEHS particles. The conditions were 7 kV charging voltage, 1 kV collecting voltage, 1 m/s face velocity, and 1 mm electrode spacing. The system was operated for 8 h per day. Error bars represent the standard deviation of the daily measurements.

[57,58]. In this work, the long-term daily average removal efficiencies for 0.3–0.5 μm, 0.5–1 μm, and 1–3 μm particles remained high at 97.7%, 98.5%, and 99.0%, respectively. The efficiency for the most penetrating 0.3–0.5 μm particles decreased by 5.4% over 14 days, representing a slightly more pronounced decline than the 7.8% degradation observed over 35 days for NaCl particles in our previous study [22]. The accelerated efficiency degradation observed for DEHS particles, relative to NaCl, can potentially be ascribed to the intrinsic physicochemical properties and distinct deposition behaviors of oily aerosols, specifically regarding the following three aspects: (1) Oil film formation. The deposition of DEHS on the collection electrodes typically forms a continuous, fluid oil film, while localized accumulation in specific areas results in the formation of large droplets (Supplementary Fig. S6). These deposits significantly weaken the discharge strength [58–60]. (2) Re-entrainment dynamics. Unlike solid particles, whose deposition film typically forms chain-like dendritic structures that induce localized electric field intensification and mitigate re-entrainment, the smooth oil film lacks these morphological advantages [61,62]. (3) Back electric field effects. Due to the lower dielectric constant and extremely low electrical conductivity, DEHS particles promote substantial surface charge accumulation. This generates a robust back electric field, which subsequently reduces the migration velocity of incoming particles within the electric field [63,64].

To restore electrode performance, a sequential cleaning procedure was employed: 10 min of ultrasonic cleaning in anhydrous ethanol followed by 2 min in deionized water, after which the electrodes were dried at ambient temperature. This cleaning procedure effectively removes the deposited oil film while ensuring that the collecting electrodes and PET coatings remain structurally intact and undamaged. The post-washing performance test demonstrated complete restoration of the collection efficiency. Specifically, the efficiency for 0.3–0.5 μm particles reached 99.3%, which is nearly identical to the initial value. This exceptional regenerative capacity demonstrates robust reusability. The SEM characterization of the electrode surface before and after washing is shown in Supplementary Fig. S7. The complete removal of accumulated particles indicates good performance under repeated washing cycles. Besides post-washing performance, PET coating stability and charging electrode aging also affect long-term performance. The hydrolytic degradation of PET is very slow under typical fluctuating indoor conditions at room temperature, and its lifetime can extend to several decades [65]. Under the complex circumstances in this work, the stability requires further characterization in future studies. In addition, efficiency degradation caused by electrode contamination can be potentially eliminated by particle-free external air protection [58]. Therefore, the proposed ESP offers the potential for sustained operational stability in long-term real-world applications.

4. Conclusions

In conclusion, this study delineates the principles of ESP performance enhancement and proposes a dielectric coating strategy to increase the breakdown voltage, enabling high-efficiency ESP operation with broad-spectrum effectiveness across diverse particle sources. The PET coating increased the breakdown voltage by up to 1.8 times on average under variable electrode spacing. The enhancement in ESP performance was quantitatively attributed to geometrical and electrohydrodynamic effects represented by the dimensionless effective area A^* and dimensionless effective migration velocity u^*. Theoretical and experimental results showed good agreement. The trade-off between efficiency and pressure drop was characterized, and a 2 mm electrode spacing is recommended when energy costs are considered. The proposed modified charge-to-diameter ratio $C_c \cdot q/d_p$ successfully characterized the efficiency minimum around 0.3–0.5 μm particles and provided a robust index for predicting size-dependent ESP performance. The broad-spectrum particle removal capability was validated using five representative particle sources. The collection efficiency followed the order of Fe > Fe_2O_3 > NaCl > DEHS, primarily governed by particle dielectric constants, whereas the ranking for indoor ambient particles varied due to their heterogeneous composition. A high removal efficiency of 99.9% was achieved for all particle sources at a collecting voltage of 1 kV. Long-term testing demonstrated stable ESP performance, with only a 5.4% reduction in oil particle efficiency over 14 days and complete recovery after washing, confirming strong reusability and practical applicability. The proposed ESP showed high efficiency, verified operational stability, and reliable broad-spectrum effectiveness for practical application in ventilation and indoor air purification systems, contributing to the development of sustainable and healthy indoor environments.

Declaration of competing interest

The authors declare that they have no known competing financial

interests or personal relationships that could have appeared to influence the work reported in this paper.

Acknowledgments

This work was supported by the National Natural Science Foundation of China (No. 52325801).

Appendix A. Supplementary data

Supplementary data to this article can be found online at https://doi.org/10.1016/j.seppur.2026.138925.

Data availability

Data will be made available on request.

References

[1] N. Liu, W. Liu, F. Deng, et al., The burden of disease attributable to indoor air pollutants in China from 2000 to 2017, Lancet Planet. Heath 7 (11) (2023) e900–e911, https://doi.org/10.1016/S2542-5196(23)00215-2.
[2] W. Yang, B. Zhao, A real-time personal PM2.5 exposure monitoring system and its application for college students, Build. Simul. 17 (9) (2024) 1531–1539, https://doi.org/10.1007/s12273-024-1163-0.
[3] T. Yu, Y. Jiang, R. Chen, et al., National and provincial burden of disease attributable to fine particulate matter air pollution in China, 1990–2021: an analysis of data from the global burden of disease study 2021, Lancet Planet. Heath 9 (3) (2025) e174–e185, https://doi.org/10.1016/S2542-5196(25)00024-5.
[4] M. Stafoggia, B. Oftedal, J. Chen, et al., Long-term exposure to low ambient air pollution concentrations and mortality among 28 million people: results from seven large European cohorts within the ELAPSE project, Lancet Planet. Heath 6 (1) (2022) e9–e18, https://doi.org/10.1016/S2542-5196(21)00277-1.
[5] L. Chu, X. Huang, D. Kong, et al., Finer particulate matter exposure disparities exist but vary across pollution concentrations, Environ. Sci. Technol. 60 (12) (2026) 8934–8943, https://doi.org/10.1021/acs.est.5c06203.
[6] C.J.L. Murray, A.Y. Aravkin, P. Zheng, et al., Global burden of 87 risk factors in 204 countries and territories, 1990–2019: a systematic analysis for the global burden of disease study 2019, Lancet 396 (10258) (2020) 1223–1249, https://doi.org/10.1016/S0140-6736(20)30752-2.
[7] Z.S. Zomorodian, M. Tahsildoost, M. Hafezi, Thermal comfort in educational buildings: a review article, Renew. Sustain. Energy Rev. 59 (2016) 895–906, https://doi.org/10.1016/j.rser.2016.01.033.
[8] J. Fang, R. Choudhary, A. Goyal, et al., From static to adaptive: a physics- and data-driven virtual testing framework for retro-commissioning of HVAC systems, Energy Use 2 (1) (2026) 100039-14, https://doi.org/10.59717/ipj.energy-use.2026.100039.
[9] A. Afshari, L. Ekberg, L. Forejt, et al., Electrostatic precipitators as an indoor air cleaner—a literature review, Sustainability 12 (21) (2020) 8774, https://doi.org/10.3390/su12218774.
[10] A.E. De Oliveira, V.G. Guerra, Electrostatic precipitation of nanoparticles and submicron particles: review of technological strategies, Process Safety Environ. Protect. 153 (2021) 422–438, https://doi.org/10.1016/j.psep.2021.07.043.
[11] E. Tian, Q. Chen, Y. Gao, et al., Advancing indoor air purification by mass transfer enhancement: bridging the gap between high-performance materials and technologies, Engineering (2025), https://doi.org/10.1016/j.eng.2025.07.003.
[12] Y. Zhu, M. Gao, M. Chen, et al., Numerical simulation of capture process of fine particles in electrostatic precipitators under consideration of electrohydrodynamics flow, Powder Technol. 354 (2019) 653–675, https://doi.org/10.1016/j.powtec.2019.06.038.
[13] Y. Zhu, C. Chen, J. Shi, et al., Enhancement of air purification by unique W-plate structure in two-stage electrostatic precipitator: a novel design for efficient capture of fine particles, Adv. Powder Technol. 31 (4) (2020) 1643–1658, https://doi.org/10.1016/j.apt.2020.02.003.
[14] T.-Y. Wen, Q.-Z. Xue, Capturing heavy loading microparticles using electrostatic precipitator with square-wave collecting electrode, Powder Technol. 361 (2020) 520–528, https://doi.org/10.1016/j.powtec.2019.11.083.
[15] T.-Y. Wen, I. Krichtafovitch, A.V. Mamishev, Numerical study of electrostatic precipitators with novel particle-trapping mechanism, J. Aerosol Sci. 95 (2016) 95–103, https://doi.org/10.1016/j.jaerosci.2016.02.001.
[16] Y. Shen, Y. Tong, Y. Zhao, et al., Experimental and computational study on the separation performance of an electrostatic precipitator with curved transvers collecting plates, Adv. Powder Technol. 32 (6) (2021) 1858–1868, https://doi.org/10.1016/j.apt.2021.03.021.
[17] L. Chen, E. Gonze, M. Ondarts, et al., Electrostatic precipitator for fine and ultrafine particle removal from indoor air environments, Sep. Purif. Technol. 247 (2020) 116964, https://doi.org/10.1016/j.seppur.2020.116964.
[18] Y. Tian, M. Li, Y. Fu, et al., Development and experimental investigation of the narrow-gap coated electrostatic precipitator with a shield pre-charger for indoor air cleaning, Sep. Purif. Technol. 309 (2023) 123114, https://doi.org/10.1016/j.seppur.2023.123114.
[19] Y. Wang, M. Yang, Z. Wu, et al., Direct observation of particle clustering and gas breakdown in charged granular streams, Powder Technol. 449 (2025) 120346, https://doi.org/10.1016/j.powtec.2024.120346.
[20] W. Xiong, Z. Lin, W. Zhang, et al., Experimental and simulation studies on dust loading performance of a novel electrostatic precipitator with dielectric barrier electrodes, Build. Environ. 144 (2018) 119–128, https://doi.org/10.1016/j.buildenv.2018.08.008.
[21] J. Mo, E. Tian, J. Pan, New electrostatic precipitator with dielectric coatings to efficiently and safely remove sub-micro particles in the building environment, Sustain. Cities Soc. 55 (2020) 102063, https://doi.org/10.1016/j.scs.2020.102063.
[22] X. Liu, Y. Gao, J. Mo, et al., Sub-kilovolt electrostatic precipitation for efficient and safe removal of airborne particles, Sep. Purif. Technol. 361 (2025) 131251, https://doi.org/10.1016/j.seppur.2024.131251.
[23] X. Xu, C. Zheng, P. Yan, et al., Effect of electrode configuration on particle collection in a high-temperature electrostatic precipitator, Sep. Purif. Technol. 166 (2016) 157–163, https://doi.org/10.1016/j.seppur.2016.04.039.
[24] Y. Zhou, Y. Liu, Z. Shi, et al., Enhanced size-dependent efficiency of removal of ultrafine particles: new solution of two-stage electrostatic precipitator with thermophoresis, Sep. Purif. Technol. 346 (2024) 127479, https://doi.org/10.1016/j.seppur.2024.127479.
[25] H. Bin, Y. Yang, Z. Lei, et al., Experimental and DFT studies of PM2.5 removal by chemical agglomeration, Fuel 212 (2018) 27–33, https://doi.org/10.1016/j.fuel.2017.09.121.
[26] D. Zhou, Z. Luo, J. Jiang, et al., Experimental study on improving the efficiency of dust removers by using acoustic agglomeration as pretreatment, Powder Technol. 289 (2016) 52–59, https://doi.org/10.1016/j.powtec.2015.11.009.
[27] Z. Sun, L. Yang, H. Wu, et al., Agglomeration and removal characteristics of fine particles from coal combustion under different turbulent flow fields, J. Environ. Sci. 89 (2020) 113–124, https://doi.org/10.1016/j.jes.2019.10.004.
[28] J.-N. Fan, Y. Yang, Y. Wang, et al., Intense field dielectric purification of oil droplets in machining buildings, J. Build. Eng. 84 (2024) 108543, https://doi.org/10.1016/j.jobe.2024.108543.
[29] H. Cao, Y. Jiang, Y. Wang, et al., A numerical simulation study on the effectiveness of a two-stage electrostatic precipitator in removing residential submicron-sized cooking particles, Adv. Powder Technol. 36 (12) (2025) 105117, https://doi.org/10.1016/j.apt.2025.105117.
[30] L. Wang, J. Morán, B.A. Olson, et al., Aerodynamic size-dependent collection and inactivation of virus-laden aerosol particles in an electrostatic precipitator, Environ. Sci. Technol. 58 (38) (2024) 16941–16951, https://doi.org/10.1021/acs.est.4c03820.
[31] F. Di Natale, L. Manna, F. La Motta, et al., Capture of bacterial bioaerosol with a wet electrostatic scrubber, J. Electrostat. 93 (2018) 58–68, https://doi.org/10.1016/j.elstat.2018.04.003.
[32] Y.-T. Chen, C.-L. Lu, S.-J. Lu, et al., Electrostatic precipitator design optimization for the removal of aerosol and airborne viruses, Sustainability 15 (10) (2023) 8432, https://doi.org/10.3390/su15108432.
[33] J. He, M. Cao, H. Xu, et al., Dual-zone electrostatic assisted filters: quantifying corona charging vs polarizing effects on bacterial disinfection across diverse species, Build. Environ. 287 (2026) 113911, https://doi.org/10.1016/j.buildenv.2025.113911.
[34] N. Čajová Kantová, A. Backa, R. Cibula, et al., Influence of biomass pellet composition on particulate matter and electrostatic precipitator efficiency, ACS Omega 10 (45) (2025) 55054–55062, https://doi.org/10.1021/acsomega.5c09639.
[35] Y. Song, Y. Zhang, Y. Liu, et al., Numerical simulation of the collection efficiency of welding fume particles in electrostatic precipitator, Powder Technol. 415 (2023) 118173, https://doi.org/10.1016/j.powtec.2022.118173.
[36] Z. Long, Q. Yao, Evaluation of various particle charging models for simulating particle dynamics in electrostatic precipitators, J. Aerosol Sci. 41 (7) (2010) 702–718, https://doi.org/10.1016/j.jaerosci.2010.04.005.
[37] R. Cochet, Lois charge des fines particules (submicroniques) etudes théoriques-controles récents spectre de particules, Coll. Int. la Phys. des Forces Electrostatiques Leurs Appl. Cent. Natl. la Rech. Sci. Paris 102 (1961) 331–338.
[38] A. Moshfegh, M. Shams, G. Ahmadi, et al., A new expression for spherical aerosol drag in slip flow regime, J. Aerosol Sci. 41 (4) (2010) 384–400, https://doi.org/10.1016/j.jaerosci.2010.01.010.
[39] R.G. Silva Araújo Andrade, M. Ondarts, B. Golly, et al., A semi-analytical model for assessing nanoparticle collection efficiencies in the partial charging regime, Sep. Purif. Technol. 379 (2025) 134972, https://doi.org/10.1016/j.seppur.2025.134972.
[40] Y. Gao, J. Wang, E. Tian, et al., Electric-field activating on-surface tailored (OST) coarse polyester fibers for efficient airborne particle removal: interfacial morphologies and electrical response, Sep. Purif. Technol. 353 (2025) 128291, https://doi.org/10.1016/j.seppur.2024.128291.
[41] Y. Gao, E. Tian, J. Mo, Electrostatic polydopamine-interface-mediated (e-PIM) filters with tuned surface topography and electrical properties for efficient particle capture and ozone removal, J. Hazard. Mater. 441 (2023) 129821, https://doi.org/10.1016/j.jhazmat.2022.129821.
[42] D. Roy, E.S. Lyou, J. Kim, et al., Commuters health risk associated with particulate matter exposures in subway system – globally, Build. Environ. 216 (2022) 109036, https://doi.org/10.1016/j.buildenv.2022.109036.
[43] K. Van Ryswyk, A.T. Anastasopolos, G. Evans, et al., Metro commuter exposures to particulate air pollution and PM2.5-associated elements in three Canadian cities:

the urban transportation exposure study, Environ. Sci. Technol. 51 (10) (2017) 5713–5720, https://doi.org/10.1021/acs.est.6b05775.
[44] T. You, Y. Zhang, Z. Sun, et al., High-speed railway thermal management for sustainable future transportation, Energy Use 1 (2) (2025) 100024-15, https://doi.org/10.59717/ipj.energy-use.2025.100024.
[45] Y. Sheng, L. Zhang, Y. Wang, et al., Exploration of a novel three-dimensional knitted spacer air filter with low pressure drop on cooking fume particles removal, Build. Environ. 177 (2020) 106903, https://doi.org/10.1016/j.buildenv.2020.106903.
[46] X. Wei, Y. Liu, H. Zhou, et al., Substantial improvement of oil aerosol filtration performance using in-plane asymmetric wettability, ACS Appl. Mater. Interfaces 12 (25) (2020) 28852–28860, https://doi.org/10.1021/acsami.0c06349.
[47] X. Liu, C.J.M. Hessels, N.G. Deen, et al., CFD-DEM investigation on the agglomeration behavior of micron-sized combusted iron fines, Fuel 346 (2023) 128219, https://doi.org/10.1016/j.fuel.2023.128219.
[48] J. Li, J. Kong, S. He, et al., Self-agglomeration mechanism of iron nanoparticles in a fluidized bed, Chem. Eng. Sci. 177 (2018) 455–463, https://doi.org/10.1016/j.ces.2017.11.038.
[49] D. Xu, Z. Hu, L.A. Zhang, et al., Study on dynamic characteristics of magnetic coagulation of Fe-based fine particles in iron and steel industry, Atmosphere 14 (9) (2023), https://doi.org/10.3390/atmos14091434.
[50] Dielectric constant values for common materials, 2026 https://www.clippercontrols.com/technotes/dielectric-constant-values. (Accessed 2026-04-03).
[51] P. Intra, Development and performance evaluation of a fast-response electrostatic sensor for sub-micrometer particle number concentration, J. Electrostat. 140 (2026) 104260, https://doi.org/10.1016/j.elstat.2026.104260.
[52] W.G. Shin, C. Qi, J. Wang, et al., The effect of dielectric constant of materials on unipolar diffusion charging of nanoparticles, J. Aerosol Sci. 40 (5) (2009) 463–468, https://doi.org/10.1016/j.jaerosci.2009.01.003.
[53] B.J. Yoon, Continuum theory for ionic field charging of spheroidal aerosols in nonuniform electric field, Chem. Eng. Sci. 55 (22) (2000) 5485–5495, https://doi.org/10.1016/S0009-2509(00)00172-X.
[54] World-Health-Organization, WHO global air quality guidelines. https://www.who.int/publications/i/item/9789240034228, 2021. (Accessed 27 May 2026).
[55] N. Cid, J.J. Rico, R. Pérez-Orozco, et al., Experimental study of the performance of a laboratory-scale ESP with biomass combustion: discharge electrode disposition, dynamic control unit and aging effect, Sustainability 13 (18) (2021) 10344, https://doi.org/10.3390/su131810344.
[56] S. Sander, U. Fritsching, Dynamic flowsheet simulation of re-entrainment from particle layers formed inside electrostatic precipitators, Particuology 53 (2020) 41–47, https://doi.org/10.1016/j.partic.2019.12.009.
[57] T. Czech, A. Marchewicz, A.T. Sobczyk, et al., Discharge electrode degradation in dry electrostatic precipitator cleaning of exhaust gases from industrial solid waste incinerators, Appl. Sci. 14 (17) (2024) 7616, https://doi.org/10.3390/app14177616.
[58] Y. Gu, E. Tian, F. Xia, et al., A new pin-to-plate corona discharger with clean air protection for particulate matter removal, Energy Built Environ. 1 (1) (2020) 87–92, https://doi.org/10.1016/j.enbenv.2019.11.006.
[59] S. Zhang, W. Pan, H. Zhang, et al., High-efficient removal of airborne oil mist in a wire-plate electrostatic precipitator, J. Electrostat. 108 (2020) 103516, https://doi.org/10.1016/j.elstat.2020.103516.
[60] H. Gao, Z. Long, Z. Feng, et al., Numerical simulation of the characteristics of oil mist particles deposition in electrostatic precipitator, Process Saf. Environ. Prot. 164 (2022) 335–344, https://doi.org/10.1016/j.psep.2022.06.022.
[61] S. Tao, Y. Zhu, M. Chen, et al., Mechanism of submicron particle dendrite agglomeration growth and fracture in flow-electric coupling field, Chem. Eng. Sci. 296 (2024) 120213, https://doi.org/10.1016/j.ces.2024.120213.
[62] Y. Zhu, Z. Huang, S. Tao, et al., Re-entrainment mechanism of submicron particles during electrostatic capture process, Chem. Eng. Sci. 308 (2025) 121417, https://doi.org/10.1016/j.ces.2025.121417.
[63] C. Zheng, H. Zhang, X. Liu, et al., Effect of dust layer in electrostatic precipitators on discharge characteristics and particle removal, Fuel 278 (2020) 118335, https://doi.org/10.1016/j.fuel.2020.118335.
[64] P. Bürger, U. Riebel, Formation of highly resistive SiO2 nanoparticle layers from the aerosol by electrostatic precipitation at 200°C: observations on back corona and nanoparticle layer structure, J. Nanopart. Res. 23 (8) (2021) 165, https://doi.org/10.1007/s11051-021-05292-4.
[65] F. Dubelley, E. Planes, C. Bas, et al., Predictive durability of polyethylene terephthalate toward hydrolysis over large temperature and relative humidity ranges, Polymer 142 (2018) 285–292, https://doi.org/10.1016/j.polymer.2018.03.043.